npj computational materials

www.nature.com/npjcompumats

ARTICLE OPEN

Check for updates

Accurate prediction of oxygen vacancy concentration with disordered A-site cations in high-entropy perovskite oxides

Jiyun Park[1], Boyuan Xu[2], Jie Pan[3], Dawei Zhang[4], Stephan Lany[5], Xingbo Liu[6], Jian Luo[4,7] and Yue Qi[1]✉

Entropic stabilized ABO_3 perovskite oxides promise many applications, including the two-step solar thermochemical hydrogen (STCH) production. Using binary and quaternary A-site mixed $\{A\}FeO_3$ as a model system, we reveal that as more cation types, especially above four, are mixed on the A-site, the cell lattice becomes more cubic-like but the local Fe–O octahedrons are more distorted. By comparing four different Density Functional Theory-informed statistical models with experiments, we show that the oxygen vacancy formation energies (E_V^f) distribution and the vacancy interactions must be considered to predict the oxygen non-stoichiometry (δ) accurately. For STCH applications, the E_V^f distribution, including both the average and the spread, can be optimized jointly to improve $\Delta\delta$ (difference of δ between the two-step conditions) in some hydrogen production levels. This model can be used to predict the range of water splitting that can be thermodynamically improved by mixing cations in $\{A\}FeO_3$ perovskites.

npj Computational Materials (2023)9:29 ; https://doi.org/10.1038/s41524-023-00981-1

INTRODUCTION

Perovskite oxides (ABO_3) can accommodate different types of cations on A- or B-sites, thereby having great tunability in oxygen vacancy formation[1,2], which can benefit various applications such as solar thermochemical hydrogen generation[3–5], solid oxide fuel cells[6], and lithium-ion batteries[7]. In the solar thermochemical hydrogen (STCH) process, hydrogen can be produced by the two-step thermochemical redox cycle as follows[8–10]:

$$TR: ABO_{3-\delta_{GS}} \rightarrow ABO_{3-\delta_{TR}} + \frac{\Delta\delta}{2}O_2(g) \quad (1)$$

$$GS: ABO_{3-\delta_{TR}} + \Delta\delta H_2O(g) \rightarrow ABO_{3-\delta_{GS}} + \Delta\delta H_2(g) \quad (2)$$

where δ_{TR} and δ_{GS} are the oxygen non-stoichiometry at the thermal reduction (TR) condition and the gas splitting/oxidation (GS) condition in $ABO_{3-\delta}$, respectively. The $\Delta\delta$ ($=\delta_{TR}-\delta_{GS}$) is the difference in δ between the TR and GS conditions. Thermodynamically, it sets the oxygen exchange capacity of the material[11] and identifies whether water splitting is possible or not[12]. For a positive $\Delta\delta$, it can represent the ideal molar amount of H_2 produced per mole of perovskite oxide and water[13]. For this thermochemical reaction, thermodynamic properties are more important than kinetic properties at high temperatures and operational conditions[8,14–16] and the kinetic factors become dominant when the water splitting temperature is reduced[16]. Thus, even though H_2 yield is controlled by both thermodynamics and kinetics, an accurate estimation of δ is required for computational material design.

Perovskite oxides with mixed cations provide the opportunity to optimize the STCH process by tuning the oxygen vacancy formation[17,18]. Previous studies for STCH applications have been mostly limited to the binary mixing of cations on the A- and B-sites[1,19–21] or on either the A- or B-site individually[22–24]. Recent advancements in high-entropy perovskite oxides, which contain five or more principal elements on either the A-site or the B-site, have introduced more tunability for various applications[25–28]. Assuming equimolar mixing, the cation mixing entropy increases from $0.7k_B$ (k_B is Boltzmann constant) to $1.4k_B$ when the number of elements increases from two to four types. This contribution will help to stabilize the mixed structure against phase segregation, especially at higher temperatures during STCH, however, its impact on δ and H_2 generation has not been addressed. High entropy mixing will certainly impose structural distortion and variation on the charge states of multivalent lattice ions that determine the oxygen non-stoichiometry. Thus, it is worthwhile to systematically investigate how structural and oxygen non-stoichiometry change with increasing types of cations on one site, in order to take advantage of the tunability.

In this paper, we systematically compared equimolar binary and quaternary A-site mixed $AFeO_3$ systems. Namely, three binary mixed A-site perovskite oxides ($Nd_{0.5}La_{0.5}FeO_3$ (NLFO), $Sr_{0.5}La_{0.5}FeO_3$ (SLFO), and $Ba_{0.5}La_{0.5}FeO_3$ (BLFO)) and one quaternary mixed A-site ($Nd_{0.25}Sr_{0.25}Ba_{0.25}La_{0.25}FeO_3$ (NSBLFO)) perovskite oxides were used as model systems. NLFO consists of two different A^{3+} cations while SLFO, BLFO, and NSBLFO represent the mixing of 50% of A^{2+} and 50% of A^{3+} cations. Many previous density functional theory (DFT) calculations on the oxygen vacancy formation energy (E_V^f) often used ordered arrangements of cations in the mixed A-/B-site perovskite oxides[21,22,29–31], although randomly distributed cations have been experimentally found in the mixed cation perovskite oxides, especially at high-temperature[32,33]. Furthermore, Energy Dispersive X-Ray Spectroscopy typically revealed compositional homogeneity in high entropy oxides[28,34–38]. For systematical comparison, randomly distributed, or disordered, A-site cations in these systems will be modeled. The changes of E_V^f, which is associated with the atomic structures, were compared by increasing the number of elements (from 2 to 4) on the A-site while keeping the ratio of A^{2+} to A^{3+}

[1]School of Engineering, Brown University, Providence, RI 02912, USA. [2]Department of Physics, Brown University, Providence, RI 02912, USA. [3]Department of Chemical Engineering and Materials Science, Michigan State University, East Lansing, MI 48824, USA. [4]Program of Materials Science and Engineering, University of California San Diego, La Jolla, CA 92093, USA. [5]Materials Science Center, National Renewable Energy Laboratory, Golden, CO 80401, USA. [6]Department of Mechanical and Aerospace Engineering, Benjamin M. Statler College of Engineering and Mineral Resources, West Virginia University, Morgantown, WV 26506, USA. [7]Department of NanoEngineering, University of California San Diego, La Jolla, CA 92093, USA. ✉email: YueQi@brown.edu

the same. This systematical comparison, especially the structural and property changes caused by the increasing number of elements on the A-site, will serve as guidance for investigating oxygen vacancies in high entropy oxides with even more cation elements (e.g., 5 or 6).

Modeling the STCH performance requires the accurate prediction of δ under different operating conditions based on DFT computed E_V^f, which faces several specific challenges in high entropy oxides. First, mixing cations with different sizes and charge states will cause local bond distortions. Since oxygen vacancy formation is sensitive to the local environment, the randomly mixed cations on the A-site would likely cause a spread of E_V^f values, as opposed to a single value in a simple lattice, where all the oxygen vacancy sites are equivalent. Therefore, all individual oxygen vacancy sites need to be sampled in DFT calculations and the statistical distribution E_V^f will be investigated. While most of the previous models to predict δ based on DFT computed E_V^f assumed equivalent oxygen sites and utilized a constant E_V^f with no spreading[1,21,22,39–41], a statistic model is required for high entropy materials. For high-entropy alloys, recent studies have started to use configuration statistics. Daigle and Brenner[42] applied traditional Boltzmann statistics to each site configuration and summed all the configurations to calculate the total vacancy concentration[42]. Recently, Chae et al.[43] simplified this approach and only used the configurations of the six nearest cations around an oxygen vacancy for high-entropy metal oxides with a rock-salt structure[43]. This method considered the non-equivalent oxygen vacancy formation energy due to local cation arrangement but may be too short range. In this study, a statistic model was derived focusing on the oxygen vacancy formation energy statistics in mixed cation systems. We will refer to this model as the high entropy (HE) model and the traditional equal oxygen site model as the low entropy (LE) model. Here the entropy refers to the cation mixing entropy and its impact on the E_V^f distribution and ultimately the δ, instead of the oxygen vacancy formation entropy (See Methods Section).

Secondly, a high oxygen vacancy concentration at the TR condition (high temperature and low oxygen partial pressure) is desired for better STCH performance. This may lead to oxygen vacancy interaction, characterized by higher oxygen vacancy formation energy with increasing oxygen nonstoichiometry, such as in $SrFe_{0.75}Mo_{0.25}O_{3-\delta}$[44], which is more complicated due to B site mixing and competition of different d-electron configurations[45]. For simpler A-site mixed ferrite, the oxygen vacancy interaction has also been investigated previously in $La_xSr_{1-x}FeO_{3-\delta}$ (x=0, 0.5, and 1)[31,46]. The oxygen vacancy repulsion is due to the excess electrons left on the lattice upon oxygen vacancy formation. The excess electron distribution can be either localized at the first two nearest neighbor Fe atoms (e.g., $LaFeO_3$[31,45]) or delocalized (e.g., in $La_{0.5}Sr_{0.5}FeO_3$ and in $SrFeO_3$[46]), depending on the cations in the systems. The excess electrons and the local bond distortion associated with an oxygen vacancy are defined as oxygen vacancy polaron. Das et al. have previously correlated the onset of the oxygen vacancy interaction with the vacancy distance approaching the polaron size. Specifically, the oxygen vacancy polaron size could be as large as ~ 8.3 Å in ferrite perovskites depending on the type of A-site cations and the crystal structures, and that the oxygen vacancies start to interact when $\delta > 0.05$[31,46]. Thus, the non-interacting and dilute limit approximation, often used in past modeling efforts[1,22,40,41], could lead to inaccurate vacancy concentrations at the TR condition, where the δ can readily exceed the dilute limit. Recently, several methods were proposed to predict δ under non-dilute limitations by using concentration-dependent vacancy formation free energy[46], large sampling[47], and shifting the Fermi level due to defect concentrations[48]. In the current work, we simplified the vacancy interaction by a linear interaction model to capture the concentration-dependent oxygen vacancy formation energy, $E_V^f(\delta) = E_V^{f,d} + \alpha \cdot \delta$, where $E_V^{f,d}$ is the vacancy formation for the dilute system, and α is a constant. To obtain $E_V^{f,d}$, we choose a simulation cell dimension of $11 \times 11 \times 16$ Å (shown in Fig. 1a), which is beyond the vacancy interaction distance in all three directions. The simulation cell contains 160 atoms, so the oxygen vacancy concentration is about 1% and the corresponding δ is 0.03, well below the dilute limit (according to previous studies in ordered $La_xSr_{1-x}FeO_3$). The interacting coefficient α was obtained from fitting DFT results, it can be compared with experimental results[16]. This linear approach was used to predict high temperature δ for $SrFeO_{3-\delta}$[46]. Overall, four models (LE-Dil, LE-Int, HE-Dil, and HE-Int), listed in Table 1, will be compared with experimentally measured δ and $\Delta\delta$ values to calibrate the validity of these models and their assumptions (See "Methods" section for details).

RESULTS

Structural characterization of randomly mixed perovskites

The effects of mixed A-site cations on structural properties were first investigated. Figure 1a shows a representative simulation cell with 32 FeO_6 octahedra highlighted in brown (Fe) with red corners (O), the four colored sites are A-sites. The mixing can induce different behaviors of global and local structural distortions[49]. The global distortion was described by the cell distortion factor D_c, which quantifies the lattice distortion from a cubic perovskite: $D_c = \frac{(a/\sqrt{2}-a_p)^2+(b/\sqrt{2}-a_p)^2+(c/2-a_p)^2}{3a_p^2} \times 10^4$ where a_p is a pseudocubic parameter, calculated as $a_p = (a/\sqrt{2} + b/\sqrt{2} + c/2)/3$[50], where a, b, c are relaxed cell lengths (listed in Supplementary Table 4). The local distortions were estimated by the distortion of one FeO_6 octahedron and the tilting between two octahedrons, as shown in Fig. 1c. Three local octahedral distortion parameters were defined. The octahedral bond distortion (D_o) was calculated as $D_o = 1/6\Sigma\{(l_i - l_{avg})/l_{avg}\}^2$ where l_i is an individual Fe–O bond length in FeO_6 and l_{avg} is the average bond length in an individual FeO_6 octahedron[51,52]. The octahedral angle distortion was analyzed by the bond angle variance (Σ^2) using θ_{O-Fe-O}: $\Sigma^2 = \sum_{i=1}^{12}(\theta_{O-Fe-O,i} - 90)^2/11$ where $\theta_{O-Fe-O,i}$ is the individual O–Fe–O angle in each octahedron[53]. Also, the local inter-octahedral tilting was evaluated using the $\theta_{Fe-O-Fe}$ and the deviation of $\theta_{Fe-O-Fe}$ from the ideal cubic (180 °) was analyzed ($180° - \theta_{Fe-O-Fe}$).

Figure 1b shows a comparison of D_c ($D_c = 0$ for the ideal cubic structure) for single component, binary, and quaternary mixing systems. For the single component systems (Supplementary Table 2), it has been known that LFO[54] and NFO[55] have orthorhombic structures while SFO[56] and BFO[57] have cubic structures as listed in Supplementary Table 2. Accordingly, D_c of the orthorhombic LFO ($D_c = 0.23$) and NFO ($D_c = 2.12$) deviate from 0 while the cubic SFO and BFO have $D_c = 0$. For all systems with mixed A-site cations, D_c deviates from cubic. In binary mixed systems, D_c is close to the compositional average. Specifically, the lattice of NLFO shows 1.25 of D_c, which is slightly greater than a simple compositional average (1.18). The D_c for SLFO and BLFO are 0.16 and 0.15, respectively, indicating that they cannot maintain the perfect ideal cubic structure, and their D_c values are also slightly greater than their compositional averages (0.13 for both). For the quaternary mixing system, the cell distortion factor is further reduced from the binary systems to $D_c = 0.10$ which is much lower than the compositional average (0.59) and is very close to the D_c of the ideal cubic structure. There is a significant change by mixing four different cations on the A-site. The global structural distortion could be minimized and the structure of NSBLFO becomes closer to a cubic structure which is known to be the most stable perovskite structure. This result is aligned with the experimental

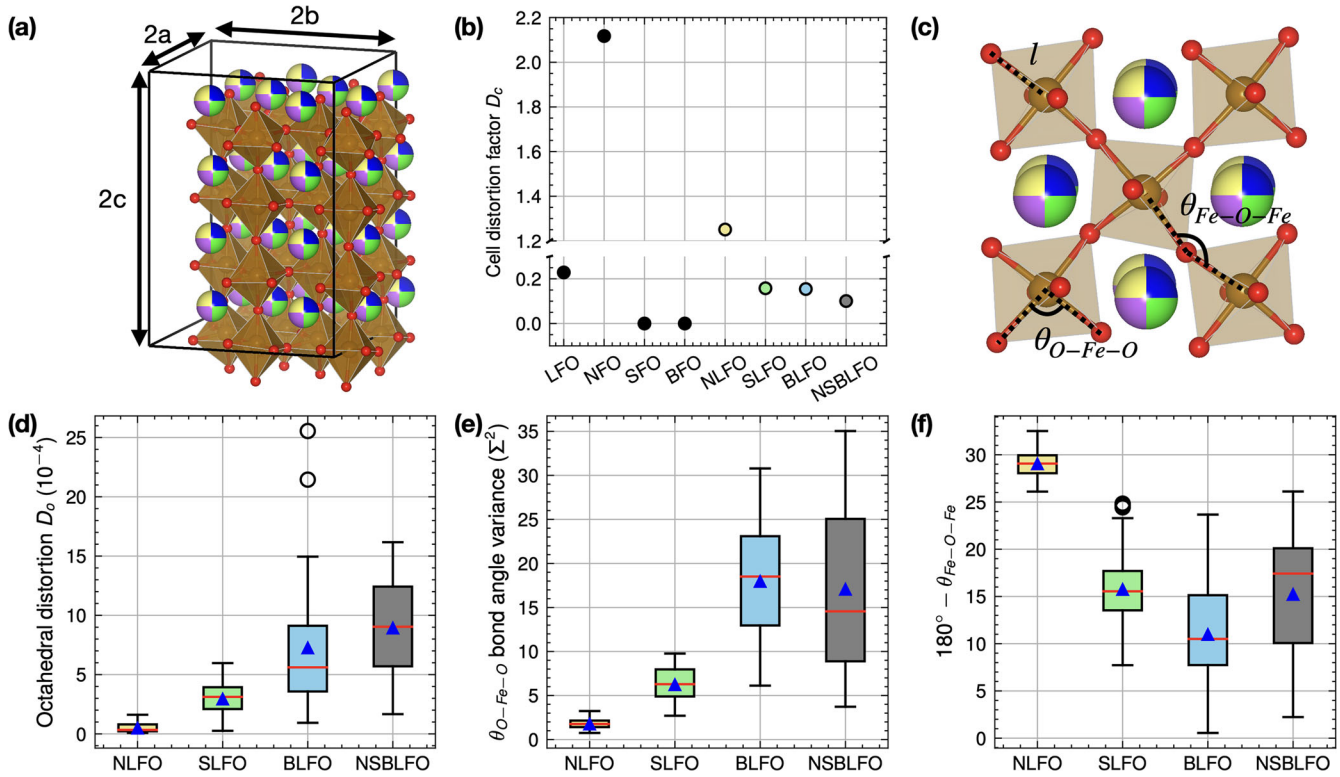

Fig. 1 Structural characterization. a Representative of the simulation cell at dimensions of ~$11 \times 11 \times 16$ Å (lattice parameters listed in Supplementary Table 4) **b** cell distortion factor D_c for different compositions, **c** representative of Fe–O bond length (l), O–Fe–O bond angle (θ_{O-Fe-O}), and Fe–O–Fe bond angle ($\theta_{Fe-O-Fe}$), **d** distribution of the octahedral distortion (D_o), **e** distribution of bond angle variance of θ_{O-Fe-O} (Σ^2), and **f** distribution of $\theta_{Fe-O-Fe}$. In **d**, **e**, and **f**, the interquartile range (difference between the top and bottom of the box) and the max-min range (difference between maximum and minimum of the extended vertical lines) are used as a measure of distribution to show how much spread out the data set is except for outliers (hollow circles). The red line and the blue triangle indicate the median and mean, respectively. More details about the boxplot are in Supplementary Fig. 4.

Table 1. A comparison of four vacancy concentration models based on oxygen vacancy formation enthalpy (ΔH_V^f) which was obtained from DFT-computed vacancy formation energies in dilute systems (E_V^f) and the thermodynamic correction for oxygen.

Models	δ expression	E_V^f or $E_{V,i}^f$ expression	Distribution of E_V^f	Vacancy interaction
LE-Dil	$3 \cdot P_s(\Delta H_V^f)$	$\overline{E}_V^f$	No	No
LE-Int	$3 \cdot P_s(\Delta H_V^f(\delta))$	$\overline{E}_V^f + a \cdot \delta$	No	Yes
HE-Dil	$3 \sum_{i=1}^{k} G(E_{V,i}^f) \cdot P_s(\Delta H_{V,i}^f)$	$E_{V,i}^f$	Yes	No
HE-Int	$3 \sum_{i=1}^{k} G(E_{V,i}^f) \cdot P_s(\Delta H_{V,i}^f(\delta))$	$E_{V,i}^f + a \cdot \delta$	Yes	Yes

$P_s(\Delta H_V^f)$ indicates the site fraction of oxygen vacancies in $\{A\}FeO_{3-\delta}$, which is about a third of the oxygen non-stoichiometry δ. The four models consider if E_V^f changes with concentration by a factor of an interacting coefficient (a) or/and has a statistical distribution ($G(E_{V,i}^f)$) in systems with mixed cations.

observation showing high-entropy mixing stabilized the cubic phase in fluorite oxides[58].

The local distortion, especially its distribution is visualized by boxplots, in Fig. 1d–f. The detailed description of a typical boxplot is in Supplementary Fig. 4. More specifically, the interquartile range (difference between upper and lower quartile) and the max-min range (difference between maximum and minimum) are used as a measure of distribution to show how spread out the data set is except for outliers. In Fig. 1d–f, the boxplots also show the median (red line), mean (blue triangle), and the outliers (empty circles) of a distribution. For the binary systems, the magnitude of the mixing effect on the local distortion varies by the type of mixing cations, especially their charge states and radius. For the NLFO, the mixing of La and Nd on the A-site makes a trivial effect on the local environments in the NLFO since Nd and La are alike. The radii of Nd^{3+} and La^{3+} are comparable (Nd^{3+} is 6.6% smaller than La^{3+} as listed in Supplementary Table 1) and their single component perovskite (LFO and NFO) has an orthorhombic structure. The average D_o and Σ^2 are respectively 0.5×10^{-9} and 1.8, which means most Fe cations are placed at the center of the FeO_6 octahedron and the octahedrons are almost undistorted. But the inter-octahedral tilting ($180° - \theta_{Fe-O-Fe}$) is maximized by mixing La and Nd cations, which agrees with the fact that the NLFO has the largest cell distortion factor D_c due to its orthorhombic nature. The distributions of all three parameters are narrower than those of other systems, implying the octahedron-to-octahedron variation is smaller. On the contrary, the BLFO shows the widest distribution among the binary systems in all three distortion parameters. That is because Ba and La are dissimilar elements in terms of size and charge state. Ba^{2+} is 18.4% larger than La^{3+} and the charge state

on Fe can be either 3+ or 4+ whose radius has a 10% difference due to the different charge state on the A-site (2+ vs. 3+) (Supplementary Table 1). Also, BFO and LFO have different crystal structures. Because of these dissimilarities between Ba and La, the local environments have a large variation shown as the wide distribution. The large D_o and Σ^2 show that the FeO_6 octahedra in BLFO are considerably distorted. However, the inter-octahedral tilting of BLFO is minimal and close to that of the ideal cubic structure possibly because the large Ba^{2+} ions expand the overall lattice and give room to the FeO_6 octahedra so that they could be well aligned. For the SLFO, the mixing effect is intermediate. The SLFO shows similar but less local distortion than the BLFO because Sr^{2+} is only 5.9% larger than La^{3+}.

For the quaternary NSBLFO system, the distributions of all local distortion parameters are wider than the binary systems indicating each FeO_6 octahedron has its own distinct local environment and the local distortion shows more variation in the quaternary system. The large average value and the wide distribution of the D_o and Σ^2 support the fact that the four different cations on the A-site disturb both bond length and bond angles of the FeO_6 octahedra more randomly and largely. The average inter-octahedral tilting angle of NSBLFO is slightly more away from the ideal cubic than that of BLFO but less away compared to the LFO and NFO systems. The FeO_6 octahedra are relatively well aligned and the inter-octahedral tilting angles have the largest variation in the NSBLFO due to the mixing of four elements. Also, the ranges of distributions of BLFO and NSBLFO are similar. This implies the effect of Ba mixing regardless of the amount of Ba is significant on the local distortion compared to the mixing of Nd or Sr due to the large Ba cation size.

Overall, the quaternary mixed NSBLFO shows the most cubic-like structure on the global scale and the largest variance of local distortions. Typical high entropy alloys often emphasize more severe lattice distortions, probably due to their simple lattice structures. Oxides have multiple sublattices for cations and anions. The effects of size mismatch and different charge states of the four elements on the A-site sublattice cause significant local distortions, but in turn, the wide range of local distortions eventually relax the cell lattice over long range. At the macroscopic scale, the NSBLFO system has the most cubic-like lattice structure, a similar trend that has been seen in some fluorite oxides as well[58]. The local distortion will impact local properties, such as oxygen vacancy formation or some catalytic behaviors, while the global cubic structure may contribute to the overall stability of the structure; highlighting the benefits of high entropy mixing.

Oxygen vacancy formation energy and its distribution

For systems with mixed cations, a first-order approximation is to take a compositional average of the DFT computed vacancy formation energies (E_V^f) of single component systems. Therefore, E_V^f for the constituent single component systems: $AFeO_3$ (A: Nd, La, Sr, and Ba) was first calculated as shown in Fig. 2a. $AFeO_3$ with trivalent A-site cations (A being Nd or La) shows 3 eV larger E_V^f compared to that with divalent cations (A being Sr or Ba), but the variation within the same type of valency is not pronounced (<1 eV). This indicates

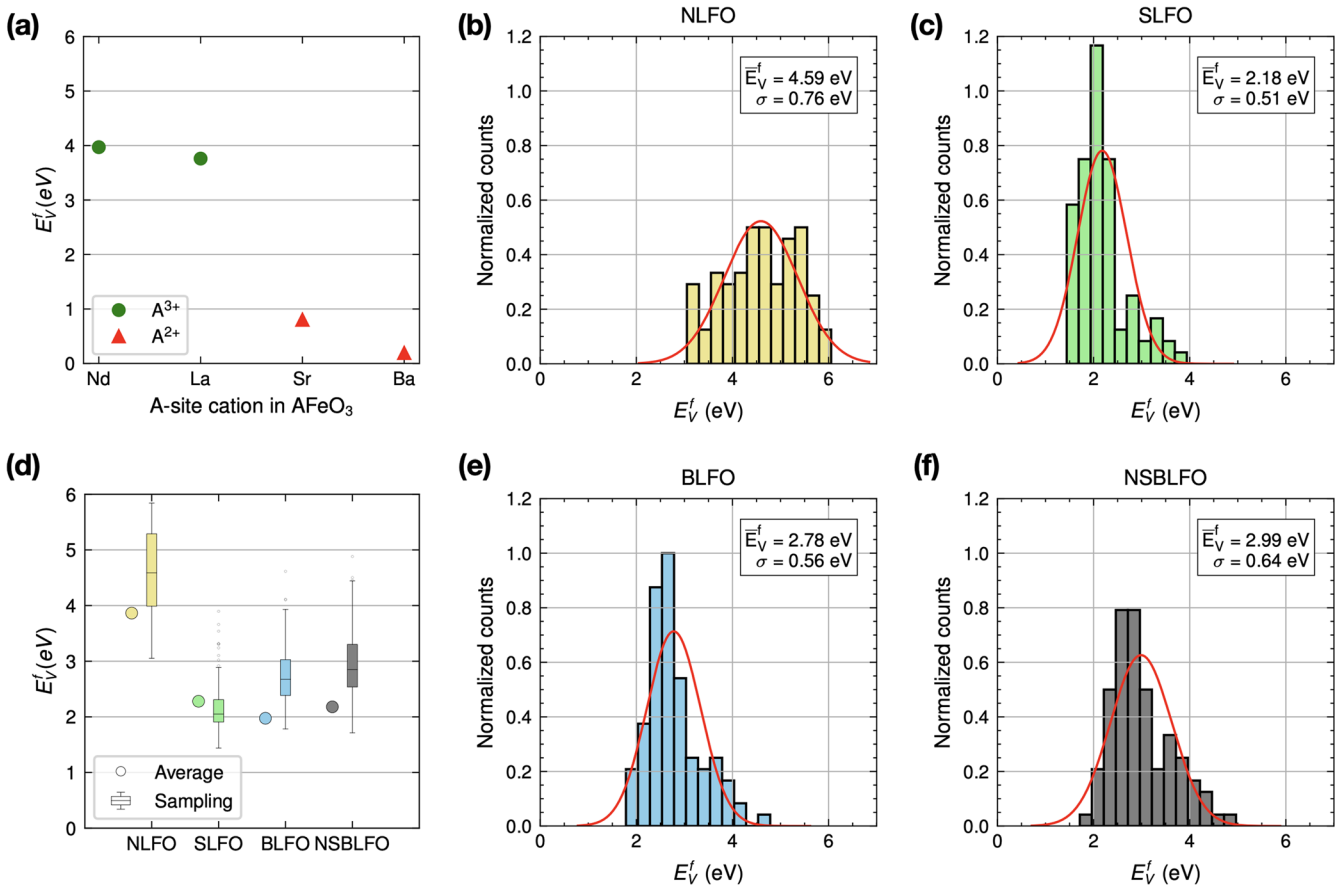

Fig. 2 Oxygen formation energy. a Single neutral oxygen vacancy formation energy (E_V^f) in the constituent single component $AFeO_3$ systems and **d** the composition weighted average E_V^f for the binary/quaternary mixed systems in circle markers and the spread of individual E_V^f in the typical box plot (see Supplementary Fig. 4). The histogram plots of oxygen vacancy formation energies for **b** NLFO, **c** BLFO, **e** SLFO, and **f** NSBLFO along with the fitted Gaussian distribution (shown in a red curve).

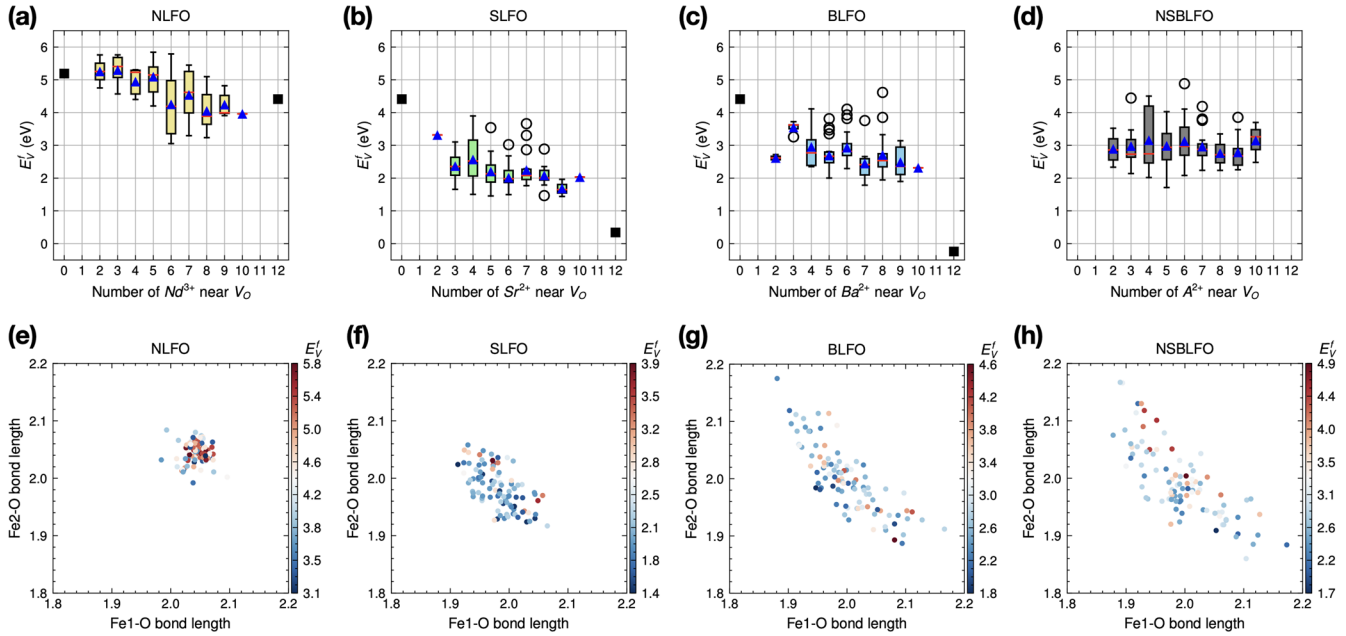

Fig. 3 Correlation of oxygen vacancy formation energy with local structures. Effect of mixing A-site cations on E_V^f for **a** NLFO, **b** BLFO, **c** SLFO, and **d** NSBLFO. The black squares indicate E_V^f in the single component system and the boxplots show the minimum, lower quartile, median (red line), upper quartile, maximum, outlier (empty circle), and mean (blue triangle) of a distribution. The oxygen vacancy formation energy versus two Fe-O bond lengths associated with each oxygen vacancy site for **e** NLFO, **f** BLFO, **g** SLFO, and **h** NSBLFO.

that the E_V^f of $AFeO_3$ is mainly controlled by the charge state on A-site cations, not by the type or by the size of the cations because the charge state on A-site determines the charge state on Fe and its electron configuration. The E_V^f for a dilute system is mainly affected by the reducibility of the Fe cation in $AFeO_3$, which is determined by its electron configuration. In a simplified picture with classical charges, Fe^{3+} ($3d^5$ electron configuration) is harder to be reduced owing to its half-filled d-orbitals, thereby showing the larger E_V^f. In contrast, Fe^{4+} ($3d^4$ electron configuration) is highly reducible to the effect that $AFeO_3$ with divalent cations has a lower E_V^f. The full picture of the DFT computed oxygen polaron size and shape for all the A cations are similar to those in the $LaFeO_3$[31,45] and in $SrFeO_3$[46], while others can be interpreted similarly to $La_xSr_{1-x}FeO_3$[46]. E_V^f values from sampling structures with randomly mixed A-site cations are visualized in histogram form (Fig. 2b, c, e and f). The mean and distribution of E_V^f values obtained from sampling are also depicted as a box plot in Fig. 2b, in comparison with the simple compositional average. The simple compositional average of four systems falls within the max-min range of boxplots (the range between the upper and lower whisker ends). However, the simple compositional average and the median value (the central line in box plots) show discrepancies that can be as large as 0.72 eV. Thus, the simple compositional average E_V^f from the single component systems does not necessarily represent the average E_V^f of the mixed systems, and using it could lead to an inaccurate estimate of related properties (e.g, δ). The box plot in Fig. 2b also shows a broader distribution of E_V^f when moving from binary SLFO and BLFO systems to quaternary NSBLFO, consistent with the broader local structure variation.

The histogram distribution of E_V^f was fit with a Gaussian distribution function as shown in red lines in Fig. 2, from which the average ($\Delta\overline{E_V^f}$) and standard deviation (σ) were obtained as annotated in Fig. 2b–f. Here, SLFO, BLFO, and NSBLFO systems will be compared due to the difference between them and the NLFO system. For SLFO, BLFO, and NSBLFO, the ratio of divalent and trivalent cations are the same, but they showed different average E_V^f and distributions. Also, the cell structure in these systems is similar to cubic structures. However, NLFO consists of two types of A^{3+} cations and its cell structure is similar to the orthorhombic structure (Fig. 1), thus it cannot be directly compared to the other three systems. For SLFO, BLFO, and NSBLFO, the larger variation in local distortion (Fig. 1d–f) results in a broader distribution (larger σ values). As the degree of local distortion spreads out, oxygen sites become diverse in terms of E_V^f, and σ increases from binary SLFO and BLFO systems to quaternary NSBLFO.

Oxygen vacancy formation energy and local structures

Since Fig. 2a shows E_V^f strongly depends on the A-site charge state in a single component $AFeO_3$, agreeing on numerous previous studies on these single or binary A-site mixed systems, such as $LaFeO_3$[31,45], $SrFeO_3$[46], and $La_xSr_{1-x}FeO_3$[46], it is natural to explore if the local chemical composition and bond lengths will affect the distribution of E_V^f. The distribution of E_V^f is likely to be correct, as to be shown in Section 2.4, they lead to predicted δ and $\Delta\delta$ values agreeing with experiments. Each O site bridges two FeO_6 octahedrons, in which each Fe cation occupies the body center of 8 A-sites; thus, the O sites can be affected by the neighboring 12 A-site cations. Figure 3a–d shows that E_V^f distribution is not strongly correlated with the number of divalent cations among those neighboring 12 A sites. For the systems having divalent cations (SLFO, BLFO, and NSBLFO), E_V^f values spread out regardless of the number of divalent cations near the oxygen vacancy site. The boxplots in Fig. 3b–d show many outliers (black circles), implying E_V^f values are not strongly tied to the number of neighboring divalent cations. For NLFO, two types of trivalent cations are mixed and its orthorhombic-like structure made the spreading of E_V^f even though it does not include divalent cations.

Additionally, the analysis of Fe–O bond lengths was conducted for all oxygen sites in the simulation cells since it has been found that the E_V^f can be affected by strain in oxides[59,60]. In the mixed A-site perovskites, two Fe–O bond lengths connecting to the Vo site do not correlate with E_V^f. Figure 3e–h shows the E_V^f value of all oxygen sites and the two corresponding Fe–O bond lengths. The color scheme indicates the E_V^f values, and E_V^f values do not show any strong correlation with the Fe–O bond lengths; rather, they are randomly distributed. In the systems with randomly mixed

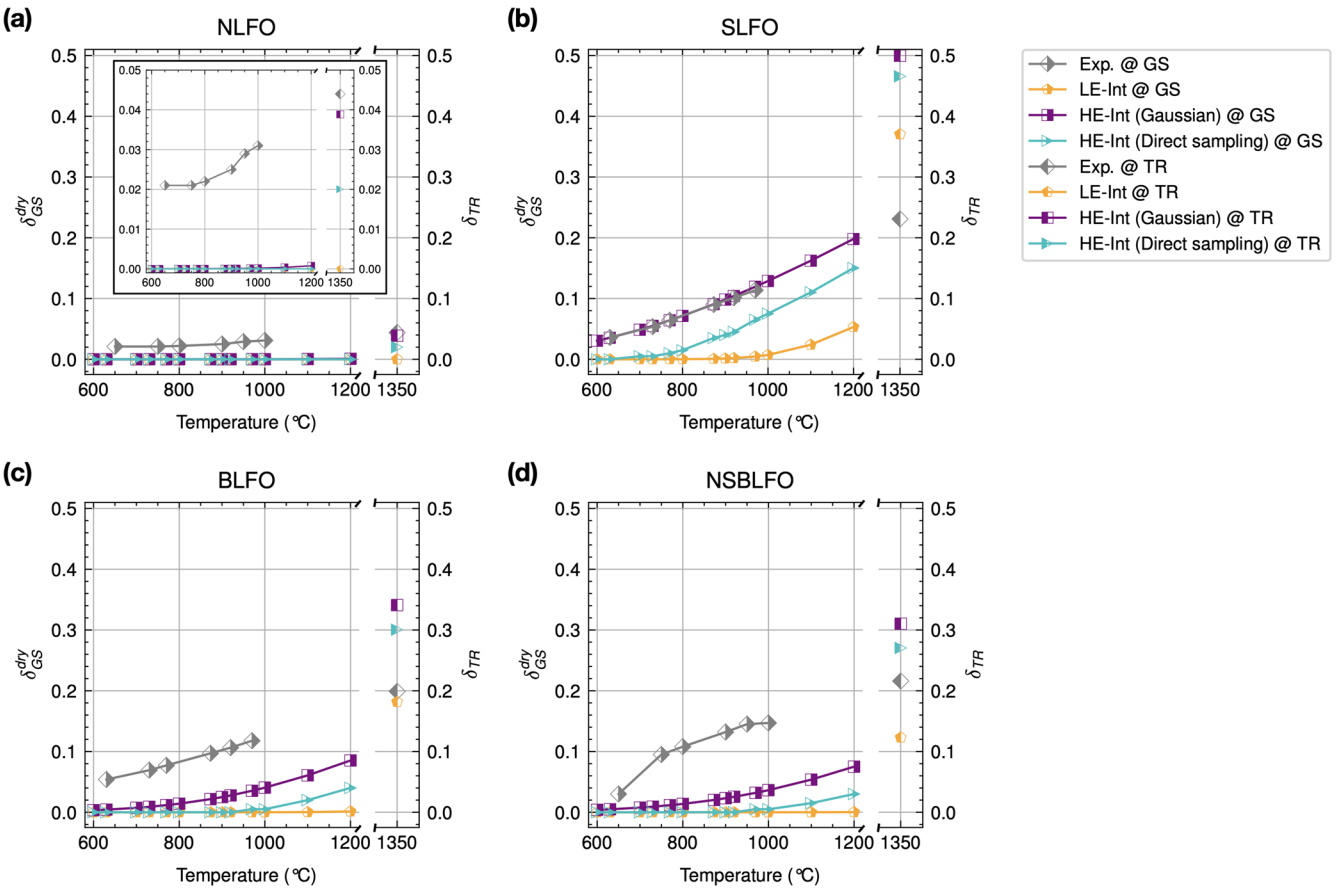

Fig. 4 Model prediction of oxygen vacancy nonstoichiometry. Comparison of δ_{GS}^{dry} and δ_{TR} between models (LE-Int and HE-Int) and experiments. The TR condition is 1350 °C with $P_{O_2} = 10^{-6}$ atm and the dry GS condition is $P_{O_2} = 0.2$ atm with varying temperatures. **a**–**d** Show δ_{TR} at the TR condition and δ_{GS}^{dry} under a range of T_{GS}. The inserted figure in **a** is a zoomed-in view.

A-site cations, our results suggest that there is no preference for E_V^f on the local chemical composition and bond lengths. It indicates that the random mixing of A-site cations leads to the spreading of E_V^f into a distribution function.

Prediction of δ and $\Delta\delta$

To validate the four models listed in Table 1, we compared their predicted δ (Fig. 4) and $\Delta\delta$ (Fig. 5) with experimental dry TGA (no hydrogen or water vapor in testing) measurements first. In the dry TGA experiment, the TR condition was 1350 °C with $P_{O_2} = 10^{-6}$ atm and the GS condition was $P_{O_2} = 0.2$ atm with varying temperatures. It is noted that the experimentally measured $\Delta\delta_{dry}$ should be more accurate than the absolute δ.

Figure 4 shows the predicted δ at the TR condition and different GS temperatures in comparison with experimental data. At GS conditions in the temperature range of 600 to 1200 °C, the HE-Int model predicted δ values that are closer to experiments for all three cases, especially for SLFO. The discrepancy in the HE-Int model could arise from the value of α, which was obtained using ordered $La_{0.5}Sr_{0.5}FeO_{3-\delta}$ structures assuming uniform vacancy distance[31]. The degree of vacancy interaction varies by materials because the size of the oxygen vacancy polaron varies. The local distortion may lead to different polaron sizes and thus the variation of oxygen vacancy interactions and α. Thus, using a material-specific α would reduce the discrepancy in BLFO and NSBLFO. In addition, the HE-Int model overestimated δ in all three cases at the TR condition, while agreeing better with the experiment for NLFO. This overestimation originates from the assumption that an oxygen vacancy occurrence at each state is considered to be an independent event, in other words, the functional form of $G(E_{V,i}^f)$ is independent of δ. However, the probability of finding an oxygen site with $E_{V,i}^f$ in a subsystem would decrease at higher δ due to vacancy interactions. This mechanism has not been implemented in the current HE-Int model and this effect can be exaggerated especially under very reducing conditions (low P_{O_2} and high temperature) when the experimental δ is above 0.2 or the computed E_V^f distribution has many low E_V^f states.

The difference in δ between TR and dry GS condition ($\delta_{TR} - \delta_{GS}^{dry}$) is expressed as $\Delta\delta_{dry}$, which is one of the parameters to evaluate water splitting performance in STCH. Based on the accuracy in predicting δ, our recently developed statistical model (HE-Int) showed improved agreement with experimental observations, especially the temperature dependence, in terms of $\Delta\delta_{dry}$. When the E_V^f is high and oxygen vacancy concentration is low (~0.05), the differences between the four models are not obvious in NLFO (Supplementary Fig. 5(a)). The non-interacting vacancy models (LE-Dil and HE-Dil) all showed unrealistically high $\Delta\delta_{dry}$ (larger than 1.5) in SLFO, BLFO, and NSBLFO (Supplementary Fig. 5), suggesting vacancy interactions must be considered for STCH applications. Therefore, only the two interacting vacancy models (LE-Int and HE-Int) are shown in Fig. 5. For the HE-Int model, both the direct sampling and Gaussian fitting methods are shown to be comparable. The calculated $\Delta\delta_{dry}$ of the LE-Int and HE-Int models at various GS temperatures and experimental values are displayed in Fig. 5b–d. The LE-Int model can be higher or lower than the experimental data and showed almost no temperature

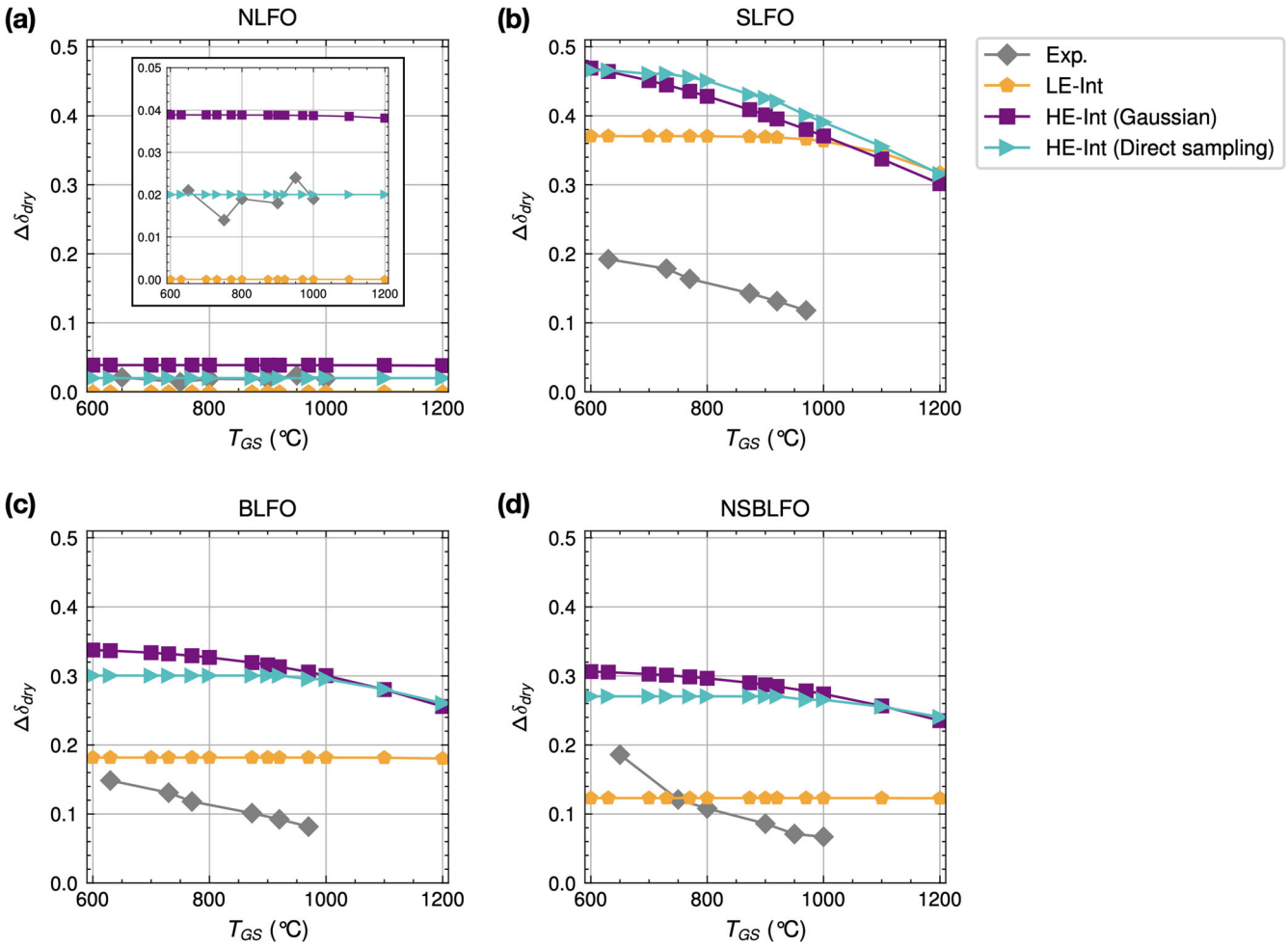

Fig. 5 Model prediction of oxygen nonstoichiometry change in STCH cycles. a–d Shows a comparison of $\Delta\delta_{dry}$ between models (LE-Int and HE-Int) and experiments in each system. The $\Delta\delta_{dry}$ is the δ difference between the TR and dry GS condition ($\Delta\delta_{dry} = \delta_{TR} - \delta_{GS}^{dry}$). The TR condition is 1350 °C with $P_{O_2} = 10^{-6}$ atm and the dry GS condition is $P_{O_2} = 0.2$ atm with varying temperatures. The inserted figure in **a** is a zoomed-in view.

dependence, thus it is not a reliable predictive model. The HE-Int model consistently showed higher $\Delta\delta_{dry}$ values than experiments and captured a similar temperature dependence trend. Therefore, the HE-Int model is more accurate and can be used to screen materials for STCH computationally.

Effects of distribution of E_V^f on $\Delta\delta$

The distribution of E_V^f (therefore, ΔH_V^f) showed several impacts on the oxygen vacancy generation and filling in STCH cycles. If all of the oxygen sites have the uniform E_V^f value, oxygen atoms would be released without any sequence. However, the presence of the distribution of E_V^f implies that the oxygen site with the lowest E_V^f would be vacant first in the TR process and filled last in the appropriate GS process. Thus, the spreading of E_V^f will enable some of the oxygen sites to be more easily utilized while the uniform E_V^f provides the equal probability of vacancy formation for all. Therefore, the impacts of E_V^f distribution on $\Delta\delta$ were investigated.

First, the HE-Int model with Gaussian distribution was used for the $\Delta\delta_{dry}$ analysis to systematically show the effect of σ (Fig. 6) since this model could predict the trend of $\Delta\delta_{dry}$ with a constant overestimation. The LE-Int model was used to show how $\Delta\delta_{dry}$ changes with E_V^f and T_{GS} with no spreading which is the same as $\sigma = 0$ in the HE-Int model with Gaussian (Fig. 6a, b). Figure 6b shows the change of $\Delta\delta_{dry}$ with E_V^f at $T_{GS} = 850$ °C annotated as a horizontal dashed line in Fig. 6a. As expected, the $\Delta\delta_{dry}$ (between the given dry TR and GS conditions) monotonically decreases as E_V^f increases. The $\Delta\delta_{dry}$ shows the most tunability when E_V^f is in the range of 1.5–3.5 eV, suggesting a target for perovskite composition design.

When the distribution of E_V^f is taken into account, the HE-Int model with Gaussian shows that the $\Delta\delta_{dry}$ is simultaneously affected by the average E_V^f and the degree of spreading of the distribution (σ) in Fig. 6c. Figure 6d shows how the $\Delta\delta_{dry}$ changes with varying σ when the average E_V^f is set to 2.60 eV. The $\Delta\delta_{dry}$ first increases when increasing spreading (σ) and is maximized when σ is 0.68. In other words, in addition to tuning the average E_V^f via cation mixing, the spreading of E_V^f distribution (σ) further increases $\Delta\delta_{dry}$ and can be optimized for a maximum $\Delta\delta_{dry}$. This can be viewed as one benefit provided by high entropy oxide design.

To further explore the benefits of increasing cation mixing entropy in STCH, $\Delta\delta$ at different $\Delta\mu_O$, which can be correlated with different equilibrium GS conditions, were plotted in Fig. 6e. The $\Delta\delta$ values are computed at different $\Delta\mu_O$ with varying σ when the average E_V^f is 2.60 eV. The $\Delta\mu_O = -1.33$ eV is the dry TGA condition (with $P_{O_2} = 0.2$ atm). At an ideal wet GS condition of $P_{H_2O} = 0.4$ atm and $P_{H_2} = 0.1$ atm (leading to 25% H_2 yield), the calculated $\Delta\mu_O$ is −3.03 eV. It is smaller than −2.86 eV of $\Delta\mu_O^{TR}$ at the TR condition, making water splitting thermodynamically

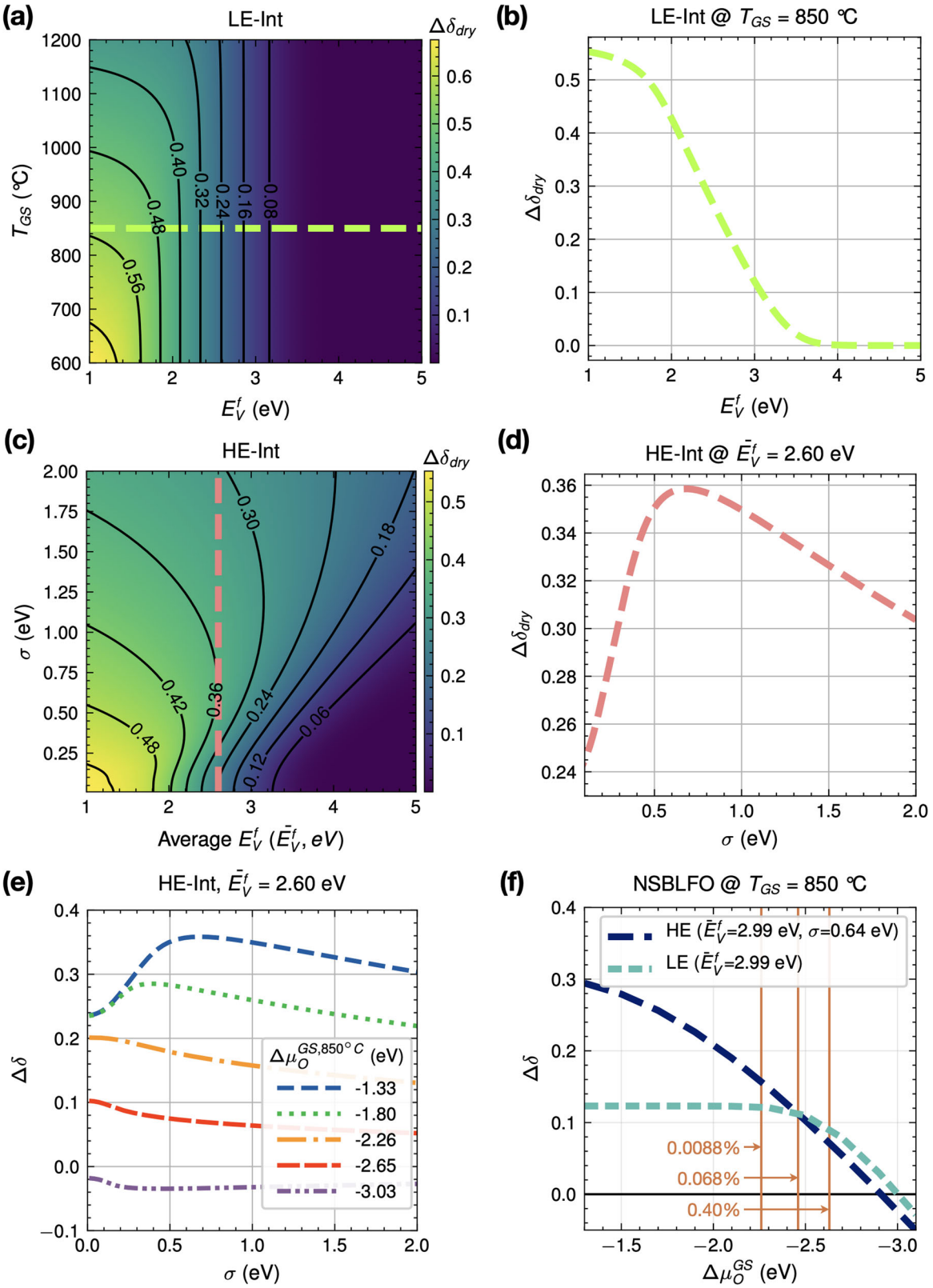

challenging[61–63], as indicated by the negative Δδ values (implying water splitting is not possible). Figure 6e shows that the gain in Δδ by the optimized spreading (σ) drops with decreasing $\Delta\mu_O$. The Δδ gain due to the spreading of the E_V^f, as shown in Fig. 6e, started to diminish at $\Delta\mu_O = -2.26$ eV, which corresponds to $P_{H_2O} = 0.4$ atm and $P_{H_2} \approx 3.5 \times 10^{-5}$ atm (0.0088% yield). This transition point of $\Delta\mu_O$ varies with both the average E_V^f and the spreading (σ) of a distribution. For instance, when the average E_V^f is 2.99 eV as seen in the case of NSBLFO, the transition from Δδ gain to no gain occurs at $\Delta\mu_O = -2.63$ eV, corresponding to $P_{H_2O} = 0.4$ atm and

Fig. 6 Improving STCH performance by tuning the distribution of oxygen vacancy formation energy. LE-Int model: **a** $\Delta\delta_{dry}$ as a function of E_V^f and T_{GS}. A solid line indicates a positive contour line and the dashed horizontal line indicates $T_{GS} = 850$ °C, and **b** the dashed curve represents $\Delta\delta_{dry}$ as a function of E_V^f at $T_{GS} = 850$ °C. HE-Int model: (**c**) $\Delta\delta_{dry}$ as a function of average E_V^f and σ. A solid line indicates a positive contour line and the dashed vertical line indicates 2.60 eV of average E_V^f, **d** the dashed curve shows $\Delta\delta_{dry}$ as a function of σ at $E_V^f = 2.60$ eV under the dry GS condition ($P_{O_2} = 0.2$ atm), and **e** trends of $\Delta\delta$ as a function of σ at $E_V^f = 2.60$ eV under wet condition at $T_{GS} = 850$ °C with different $\Delta\mu_O^{(GS,850^\circ C)}$. **f** Comparison of $\Delta\delta$ between the HE and LE models in NSBLFO (average $E_V^f = 2.99$ eV and $\sigma = 0.64$ eV) with varying $\Delta\mu_O^{(GS,850^\circ C)}$ and the vertical lines denotes H_2 yield at different $\Delta\mu_O$.

$P_{H_2} \approx 0.0016$ atm, meaning 0.4% yield (Supplementary Fig. 8). Figure 6f exemplifies NSBLFO to compare the HE-Int model with average E_V^f of 2.99 eV and σ of 0.64 eV, and the LE-Int model assuming the same average E_V^f as the HE-Int model but no spreading. The gain in $\Delta\delta$ due to the E_V^f distribution reduces as $\Delta\mu_O$ decreases until the crossover point around $\Delta\mu_O \approx$ -2.46 eV ($P_{H_2O} = 0.4$ atm and $P_{H_2} \approx 0.00027$ atm (0.068% yield)). Therefore, both the average E_V^f and the σ should be designed to maximize the gain in $\Delta\delta$ for different water splitting conditions.

DISCUSSION

STCH process is challenging because the oxygen chemical potential at the TR condition is larger than that at the GS condition if a significant H_2 yield is considered[61–63]. If the oxygen vacancy formation enthalpy is considered as an average value, a positive oxygen vacancy formation entropy of considerable magnitude is required for successful STCH materials. However, the vibrational and magnetic contributions to the vacancy formation entropy are typically small and often neglected by modeling[64–66]. Lany suggested the electronic entropy contribution from charged defect formation can be significant and should be considered[63]. Here, we showed another mechanism that the distribution of oxygen formation energy (therefore enthalpy) can lead to some H_2 production gain, especially when P_{H_2}/P_{H_2O} ratio is relatively low.

Our results showed the distribution refers to both the average and the spreading of the oxygen vacancy formation energy, which can be tuned by mixing more types of divalent and trivalent cations, and possibly at different ratios. As the number of A-site cations increases from the single component $AFeO_3$ to the quarternary mixed component $\{A\}FeO_3$, local bond distortion increases and the E_V^f distribution (fitted Gaussian) showed different average values and a larger standard deviation (single: 0; binary: 0.51 and 0.56 eV; quaternary: 0.64 eV), meaning a broader distribution.

For predicting the $\Delta\delta$, four different models were compared. Our results suggest that the E_V^f distribution as well as the interactions of oxygen vacancies must be considered to increase the accuracy of $\Delta\delta_{dry}$ prediction. Our HE-Int model with direct sampling from DFT accurately predicts the experimental observations in terms of the $\Delta\delta_{dry}$ and the δ values under the dry and wet STCH conditions. Furthermore, the HE-Int was used to explore the dependence of $\Delta\delta$ at both dry and wet STCH cycles on the distribution of E_V^f. Mixing of divalent to trivalent cations can vary the average E_V^f, generally inducing larger $\Delta\delta$. The spreading of E_V^f by mixing more types of divalent and trivalent cations on A-site further increases $\Delta\delta$, at a range of STCH conditions, especially when P_{H_2}/P_{H_2O} ratio is low.

We also have investigated the effects of mixing on the structural distortion and spreading of E_V^f in perovskites with mixed A-site cations. As the number of A-site cations increases from the single component $AFeO_3$ to the quarternary mixed component $\{A\}FeO_3$, the global lattice distortion becomes smaller and more similar to a cubic structure while the local distortions tend to vary more. However, the E_V^f distribution does not show any strong correlation with the local A-site charge distribution or the structural distortions. Rather, E_V^f values show a random distribution.

By extrapolating these results to high entropy perovskites with A-site mixing, we can expect a globally more cubic but locally more distorted structure, with a broader tunability of E_V^f distribution that can be optimized to achieve larger $\Delta\delta$ in the STCH process. Going beyond STCH applications, since the local distortions can also lead to enhanced reaction activities[67], we can envision that high entropy perovskites show even higher catalytic reactivity in oxygen reduction reaction[67] and solid oxide fuel cell applications[38].

METHODS

Randomly mixed structures

Random A-site cation distribution was generated by the special quasi-random structures (SQS) approach with the Alloy Theoretic Automated Toolkit (ATAT)[68–70] for binary and quaternary mixed A-site cations in simulation cells with 160 atoms. This simulation cell dimension (~11 × 11 × 16 Å) is large enough[71] to accommodate the oxygen vacancy polaron (with a maximum diameter of 8.3 Å in $La_{0.5}Sr_{0.5}FeO_3$[46]) and prevent their interactions. The pair correlation functions were identical to those of the theoretically random structures up to the nearest atomic shell with a distance of ~ 4 Å, indicating that A-sites in the periodic simulation cell structures are occupied by cations randomly. Due to a large possible configurational space of A-cation arrangements in binary/quaternary mixed systems and a large number of possible SQS simulation cells, three different A-cation arrangements were generated using the SQS method. To reveal the structural randomness, the A-site cation arrangements around Fe or O site were analyzed to ensure perfect random mixing of A^{2+} and A^{3+} cations in a longer range than the ~ 4 Å of distance used for the SQS. It was performed based on the hypothesis that the oxygen vacancy formation energy can be affected by the ratio of the number of nearby A^{2+} and A^{3+} cations and by the charge state of neighboring Fe sites which can be determined by nearby A cations. One Fe site (or FeO_6 octahedron) is coordinated by eight A sites, and one O site is surrounded by 12 neighboring A sites. The number of A^{2+} cations centered by O or Fe sites was analyzed in Supplementary Fig. 3, which shows the distribution follows the Gaussian distribution. It confirms the cations were randomly displaced on A-sites in the selected structures.

These three configurations were applied to both the cubic and the orthorhombic initial structures which were chosen based on the experimentally known structure of the constituent single component ABO_3: LFO[54] and NFO[55] being orthorhombic, and SFO[56] and BFO[57] being cubic. In the binary systems (NLFO, SLFO, and BLFO), three different La configurations were commonly used while varying the rest A-site cations for a fair comparison. Supplementary Fig. 1 shows all six configurations tested for BLFO, and Ba was replaced with either Nd or Sr for NLFO and SLFO, respectively. For the quarternary system, three different A-cation arrangements were used for cubic and orthorhombic structures, as shown in Supplementary Figure 2. After both ionic and cell relaxation, the energy difference (ΔE) among the six different initial structures is listed in Supplementary Table 3. The small energy difference (much less than the proposed criterion of $\Delta E < 40$ meV atom^{-1}[72] or <100 meV atom^{-1}[73] for ABO_3 compounds) suggests that the six different initial random

structures for each system are stable and thermodynamically comparable. Therefore, the structure with the minimum energy after full relaxation was selected as the representative structure of each system for structure and vacancy analysis.

DFT combined with thermodynamics

In STCH processes, perovskite oxides are exposed to high temperatures and oxygen vacancy formation enthalpy ΔH_V^f relies on the chemical potential of oxygen ($\Delta\mu_O$). Thus, we combined DFT and thermodynamic modeling. All DFT calculations for the 0 K ground state were performed using the Vienna Ab initio Simulation Package[74] with the spin-polarized generalized gradient approximation along with Perdew, Burke, and Ernzerhof (GGA-PBE) and the GGA+U method. The PAW potentials used in this study are La ($5s^2\ 5p^6\ 6s^2\ 5d^1$ of valence electronic configuration), Sr_sv ($4s^2\ 4p^6\ 5s^2$), Ba_sv ($5s^2\ 5p^6\ 6s^2$), Nd_3 ($4f^1\ 5s^2\ 5p^6\ 6s^2$), Fe_pv ($3p^6\ 3d^7\ 4s^1$), and O_s ($2s^2\ 2p^4$). Due to the large data sampling, the soft "O_s" pseudopotential was used as previously used in perovskite oxides[75–77] with the cutoff energy of 380 eV that is ~ 34% higher than the default cutoff energy[78,79]. It leads to less than 0.1 ~ 0.2 eV difference in the similar oxygen vacancy formation energy when the simulation cell consists of two and 32 formula units, compared to our previous work on $La_xSr_{1-x}FeO_3$ with the standard potential of O and Fe and higher cutoff energy of 500 eV[31,46]. The total energy and ionic force convergence criteria are 10^{-6} eV and 0.02 eV Å^{-1} respectively. A Gamma-centered k-point mesh was set to $2\times2\times1$ for the simulation cell, to ensure a k-spacing of 0.3–0.4 Å^{-1}. $U_{eff} = 3$ was chosen based on our previous extensive U parameter tests[31]. This single U parameter was able to capture the magnetic moments for Fe at a broad range of charge states, which can vary between 2+ and 4+ due to the mixing of A^{2+} and A^{3+} cations and oxygen vacancies, and gave the correct band gap and phases for various $La_xSr_{1-x}FeO_3$ compositions and phases[31].

The DFT computed formation energy of a single neutral vacancy (E_V^f) is defined as $E_V^f = E_{defective} - E_{bulk} + \mu_O^{FERE}$ where $E_{defective}$ and E_{bulk} are the DFT calculated energy of a simulation cell with and without a vacancy (V_O), respectively. All possible V_O structures were sampled using Python Materials Genomics (pymatgen)[80] and individual E_V^f was calculated for all. μ_O^{FERE} is the fitted elemental-phase reference energy (FERE) of oxygen (-4.76 eV for an oxygen atom) which was developed for accurate prediction of enthalpies of formation[81]. The free energy of oxygen vacancy formation ($\Delta G_V^f(T,P_{O_2})$) governs the vacancy concentration and it is expressed as $\Delta G_V^f(T,P_{O_2}) = \Delta H_V^f(T,P_{O_2}) - T\Delta S_V^f(T,P_{O_2})$ where $\Delta H_V^f(T,P_{O_2})$ is the oxygen vacancy formation enthalpy and the $\Delta S_V^f(T,P_{O_2})$ is the oxygen vacancy formation entropy. The vibrational entropic contributions to $\Delta S_V^f(T,P_{O_2})$ are relatively small and neglected[64–66]. The dominating contribution to $\Delta S_V^f(T,P_{O_2})$ becomes oxygen gas[82], $\Delta S_V^f(T,P_{O_2}) \approx \frac{1}{2}\Delta S_{O_2}(T,P_{O_2})$.

At a testing condition, finite temperature (T) and oxygen partial pressure P_{O_2}, $\Delta\mu_O(T,P_{O_2})$ were used as the thermodynamic correction for an isolated oxygen molecule, describing the chemical potential change from 0 K to T at P_{O_2} including the entropy of oxygen gas ($\Delta S_{O_2}(T,P_{O_2})$) as explicitly discussed in Ref. [46]. The oxygen vacancy formation enthalpy $\Delta H_V^f(T,P_{O_2})$ was calculated as follows:

$$\begin{aligned}\Delta G_V^f(T,P_{O_2}) &= \Delta H_V^f(T,P_{O_2}) - T\left(\tfrac{1}{2}\Delta S_{O_2}(T,P_{O_2})\right)\\ &= E_{defective}(T,P_{O_2}) - E_{bulk}(T,P_{O_2}) + \tfrac{1}{2}\mu_{O_2}(T,P_{O_2}) - T\left(\tfrac{1}{2}\Delta S_{O_2}(T,P_{O_2})\right)\\ &= E_{defective} - E_{bulk} + \mu_O^{FERE} + \Delta\mu_O(T,P_{O_2})\\ &= E_V^f + \Delta\mu_O(T,P_{O_2})\end{aligned} \tag{3}$$

For systems with mixed cations, an average vacancy formation energy $\overline{E_V^f}$ was used for this calculation. In experiments, various testing conditions have been used for STCH performance analysis.

Table 2. $\Delta\mu_O^{GS}$ values at different P_{O_2}, P_{H_2O}, and P_{H_2} conditions at 850 °C.

$\Delta\mu_O^{GS}$ (eV)	P_{O_2} (atm)	P_{H_2O} (atm)	P_{H_2} (atm)	Condition
−1.33	0.2	–	–	Dry
−1.80	–	0.4	~3.0×10^{-7}	Wet
−2.26	–	0.4	~3.5×10^{-5}	Wet
−2.65	–	0.4	~0.002	Wet
−3.03	–	0.4	~0.1	Wet

When water steam is not involved in the GS reaction, $\Delta\mu_O(T,P_{O_2})$ is solely determined by temperature and P_{O_2}, which will be referred to as the dry condition. For a dry condition, $\Delta\mu_O(T,P_{O_2}) = \frac{1}{2}(\Delta\mu_{O_2}^0(T) + k_BT\ln P_{O_2})$ is determined by the change in chemical potential of oxygen from 0 K to T at a given P_{O_2}, and $\Delta\mu_{O_2}^0(T)$ is calculated with the specific heat of oxygen gas at temperature T and the entropy of oxygen gas at the standard state[46]. In a wet GS condition where water steam is injected into a reactor, P_{O_2} can be calculated by using P_{H_2O} and P_{H_2} following equation:

$$\begin{aligned}\Delta\mu_O &= \Delta H_{H_2O}^f + \Delta\mu_{H_2O} - 2\Delta\mu_H\\ \Delta\mu_{H_2O} &= \Delta\mu_{H_2O}^0(T) + k_BT\ln P_{H_2O}\\ \Delta\mu_H &= \tfrac{1}{2}\left(\Delta\mu_{H_2}^0(T) + k_BT\ln P_{H_2}\right),\end{aligned} \tag{4}$$

where $\Delta H_{H_2O}^f$ is the formation enthalpy for water. Note that $\Delta H_{H_2O}^f$ was used in place of the free energy of formation ($\Delta G_{H_2O}^f$) since entropic contributions are relatively small.

In this paper, three different testing conditions for $\Delta\mu_O(T,P_{O_2})$ were used: TR, dry GS, and wet GS conditions. At the TR condition, temperature was set to 1350 °C and P_{O_2} was 0.2 atm, which gives $\Delta\mu_O^{TR} = -2.86$ eV. For the dry GS condition, a wide range of temperatures (600-1200 °C) were examined at $P_{O_2} = 0.2$ atm to analyze how δ_{GS} changes with temperature. For the wet GS condition, temperature and P_{H_2O} were set to 850 °C and 0.4 atm, respectively, and multiple P_{H_2} values were examined. The P_{H_2O} and P_{H_2} at equilibrium GS condition was also used to calculate H_2 yield as P_{H_2}/P_{H_2O} ratio. All GS conditions could be incorporated as $\Delta\mu_O^{GS}$ and Table 2 lists the GS conditions used in this paper. With the calculated E_V^f and $\Delta\mu_O$, ΔH_V^f was determined to calculate the δ in {A}FeO_3 under various conditions. The $\Delta\delta$ under dry GS condition is referred to as $\Delta\delta_{dry} (= \delta_{TR} - \delta_{GS}^{dry})$. In the actual STCH processes, water steam is involved in the GS reaction; thus, $\Delta\delta$ is described as $\delta_{TR} - \delta_{GS}^{wet}$.

DFT combined with statistics

In contrast to single component $ABO_{3-\delta}$ systems, multiple elements mixing on A- or B-sites leads to a spread of E_V^f and the corresponding ΔH_V^f; therefore, we employed a statistical approach to predict the δ using the distribution of E_V^f values. To elucidate the effects of the distribution of E_V^f along with the effects of the vacancy interaction, we compared four different models that either consider or ignore the statistical distribution of oxygen vacancy formation energy and/or oxygen vacancy interactions. The most commonly used non-interacting dilute model, referred to as LE-Dil, assumes that vacancies are non-interacting and the oxygen formation energy/enthalpy is a single value[83]. The vacancy concentration is given by $\delta/(3-\delta) = \exp(-\Delta H_V^f/(k_BT))$ where k_B is the Boltzmann constant. Thus, the δ in $ABO_{3-\delta}$ can be expressed as equation (5):

$$\delta = 3\cdot\frac{\exp\left(\frac{-\Delta H_V^f}{k_BT}\right)}{1+\exp\left(\frac{-\Delta H_V^f}{k_BT}\right)} = 3\cdot P_s\left(\Delta H_V^f\right) \tag{5}$$

where $P_s(\Delta H_V^f)$ indicates the site fraction of oxygen vacancies. This model has been used in $ABO_{3-\delta}$ oxygen vacancy

calculations[83,84] despite the fact that oxygen vacancy interactions do arise as δ increases[31,39,46,48,85,86].

Considering the interaction between vacancies, referred to as the LE-Int model, the E_V^f becomes a function of δ. A simple linear relationship was used to describe increasing E_V^f with increasing δ by a factor of an interacting coefficient, α, which can be material-dependent. In this study, the α value was set to 2.6 (eV) obtained by a linear fitting of the DFT-calculated E_V^f values from our previous $La_{0.5}Sr_{0.5}FeO_{3-\delta}$ study in Ref. [31], where an ordered arrangement of La and Sr on A-site was used.

In a system with randomly mixed cations, E_V^f becomes a distribution function, $G(E_{V,i}^f)$, which can be discretized into total k numbers of $E_{V,i}^f$ states. In this study, two approaches for $G(E_{V,i}^f)$ were used: the direct sampling method used E_V^f distribution from DFT calculation as $G(E_{V,i}^f)$ and the Gaussian distribution fitting method utilized the fitted Gaussian distribution function for $G(E_{V,i}^f)$. If an oxygen vacancy occurrence at each state is considered to be an independent event, the functional form for each subsystem that holds the vacancy state will be independent on δ. Each subsystem still takes the form of a two-level system (empty or filled sites) and the energetic preference of having a vacancy at the i state is the Boltzmann probability with a partition function $Z_i = 1 + \exp\left(\frac{-\Delta H_{V,i}^f}{k_B T}\right)$[87]. Then the probability of finding vacant oxygen sites at an energy level is $G(E_{V,i}^f) \cdot P_s(\Delta H_{V,i}^f)$. Summing all the states leads to the total number of oxygen vacancies, δ.

$$\delta = 3\sum_{i=1}^{k} G\left(E_{V,i}^f\right) \cdot P_s\left(\Delta H_{V,i}^f\right) \tag{6}$$

The statistical distribution of E_V^f was considered in both HE-Dil and HE-Int models. For the HE-Dil model, the vacancy formation enthalpy at i state, $\Delta H_{V,i}^f$, is calculated as $E_{V,i}^f + \Delta\mu(T, P_{O_2})$; but for the HE-Int model, the interaction of vacancies was implemented using the interacting coefficient α: $\Delta H_{V,i}^f = E_{V,i}^f + \Delta\mu(T, P_{O_2}) + \alpha \cdot \delta$.

Experiments

All samples were synthesized through a conventional solid-state method. The precursor powder La_2O_3 (99.99%), $SrCO_3$ (99.9%), $BaCO_3$ (99.9%), Nd_2O_3 (99.99%) and Fe_2O_3 (99.99%) were purchased from Alfa Aesar. The precursor powder was weighted and put in a poly(methyl methacrylate) high-energy ball mill (HEBM) vial with endcaps and milling balls made by tungsten carbide. The samples were dry milled for 100 min and further annealed in air at 1300 °C for 10 hours. The perovskite powder was ground by pestle and mortar for further tests.

Thermogravimetric analysis (TGA) was conducted using a simultaneous thermal analyzer (NETZSCH STA 449 F3 Jupiter). For each test, 30 mg of sample was placed on an alumina crucible. The sample was heated up to 1350 °C with a 25 °C min^{-1} ramping rate and was held isothermally for 45 min under ultra-high-purity (UHP) Ar. Then, the sample was cooled down to 1000 °C with the same ramp rate, and 21% O_2 balanced with Ar was introduced to re-oxidize the sample. The cycle was repeated for six different oxidation temperatures (1000, 950, 900, 800, 750, 650 °C). The mass loss curves of samples were calibrated by a blank crucible run. The mass loss was converted into oxygen non-stoichiometry based on the following equation:

$$\delta = \frac{\Delta m \times M_s}{m_s \times M_o} \tag{7}$$

where δ is the extent of reduction, Δm stands for the mass loss measured by the TGA, m_s is the initial mass of the specimen, and M_s and M_O represent the molar mass of the specimen and oxygen, respectively.

DATA AVAILABILITY

The data that support the findings of this study are available from the corresponding authors upon reasonable request.

CODE AVAILABILITY

Defect structures were populated using the Python Materials Genomics (pymatgen)[80]. The codes supporting the present work are available from the corresponding authors upon reasonable request.

Received: 17 August 2022; Accepted: 14 February 2023;
Published online: 28 February 2023

REFERENCES

1. Deml, A. M. et al. Tunable oxygen vacancy formation energetics in the complex perovskite oxide $Sr_xLa_{1-x}Mn_yAl_{1-y}O_3$. *Chem. Mater.* **26**, 6595–6602 (2014).
2. Heo, S. J. & Zakutayev, A. Combinatorial screening of the crystal structure in Ba–Sr–Mn–Ce perovskite oxides with ABO_3 stoichiometry. *J. Mater. Chem. A* **9**, 21032–21043 (2021).
3. Zhang, D. et al. Compositionally complex perovskite oxides for solar thermochemical water splitting. *Chem. Mater.* https://doi.org/10.1021/acs.chemmater.2c03054 (2023).
4. Cooper, T. et al. Lanthanum manganite perovskites with Ca/Sr A-site and Al B-site doping as effective oxygen exchange materials for solar thermochemical fuel production. *Energy Technol.* **3**, 1130–1142 (2015).
5. Lenarduzzi, G. & Cooper, T. A. The role of entropy in the success of non-stoichiometric oxides for two-step thermochemical water and CO_2 splitting. *Appl. Phys. Lett* **119**, 263902 (2021).
6. Shi, Y., Ni, N., Ding, Q. & Zhao, X. Tailoring high-temperature stability and electrical conductivity of high entropy lanthanum manganite for solid oxide fuel cell cathodes. *J. Mater. Chem. A* **10**, 2256–2270 (2022).
7. Yan, J. et al. A high-entropy perovskite titanate lithium-ion battery anode. *J. Mater. Sci.* **55**, 6942–6951 (2020).
8. Scheffe, J. R. & Steinfeld, A. Oxygen exchange materials for solar thermochemical splitting of H_2O and CO_2: a review. *Mater. Today* **17**, 341–348 (2014).
9. Muhich, C. L. et al. A review and perspective of efficient hydrogen generation via solar thermal water splitting. *Wiley Interdiscip. Rev. Energy Environ.* **5**, 261–287 (2016).
10. Haeussler, A., Abanades, S., Jouannaux, J. & Julbe, A. Non-stoichiometric redox active perovskite materials for solar thermochemical fuel production: a review. *Catalysts* **8**, 611 (2018).
11. Li, S. et al. Thermodynamic guiding principles for designing nonstoichiometric redox materials for solar thermochemical fuel production: ceria, perovskites, and beyond. *Energy Technol.* **10**, 2000925 (2022).
12. Bergeson-Keller, A. M., Sanders, M. D. & O'Hayre, R. P. Reduction thermodynamics of $Sr_{1-x}Ce_xMnO_3$ and $Ce_xSr_{2-x}MnO_4$ perovskites for solar thermochemical hydrogen production. *Energy Technol.* **10**, 2100515 (2022).
13. Takacs, M. et al. Oxygen nonstoichiometry, defect equilibria, and thermodynamic characterization of LaMnO3 perovskites with Ca/Sr A-site and Al B-site doping. *Acta Mater.* **103**, 700–710 (2016).
14. Davenport, T. C., Yang, C., Kucharczyk, C. J., Ignatowich, M. J. & Haile, S. M. Implications of exceptional material kinetics on thermochemical fuel production rates. *Energy Technol.* **4**, 764–770 (2016).
15. Ignatowich, M. J. et al. Impact of enhanced oxide reducibility on rates of solar-driven thermochemical fuel production. *MRS Commun.* **7**, 873–878 (2017).
16. Qian, X. et al. Favorable redox thermodynamics of $SrTi_0.5Mn0.5O_{3-\delta}$ in solar thermochemical water splitting. *Chem. Mater.* **32**, 9335–9346 (2020).
17. Zhu, H., Zhang, P. & Dai, S. Recent advances of lanthanum-based perovskite oxides for catalysis. *ACS Catal.* **5**, 6370–6385 (2015).
18. Liu, Y. et al. Recent advances in heteroatom doping of perovskite oxides for efficient electrocatalytic reactions. *Nanoscale* **13**, 19840–19856 (2021).
19. Jia, T. et al. The influence of oxygen vacancy on the electronic and optical properties of $ABO_{3-\delta}$ (A= La, Sr, B= Fe, Co) perovskites. *Phys. Chem. Chem. Phys.* **21**, 20454–20462 (2019).
20. Chen, Z. et al. Sr-and Co-doped $LaGaO_{3-\delta}$ with high O_2 and H_2 yields in solar thermochemical water splitting. *J. Mater. Chem. A* **7**, 6099–6112 (2019).
21. Maiti, D., Daza, Y. A., Yung, M. M., Kuhn, J. N. & Bhethanabotla, V. R. Oxygen vacancy formation characteristics in the bulk and across different surface terminations of $La_{(1-x)}Sr_xFe_{(1-y)}Co_yO_{(3-\delta)}$ perovskite oxides for CO_2 conversion. *J. Mater. Chem. A* **4**, 5137–5148 (2016).
22. Jia, T., Popczun, E. J., Lekse, J. W. & Duan, Y. Effective Ca^{2+}-doping in $Sr_{1-x}Ca_xFeO_{3-\delta}$ oxygen carriers for chemical looping air separation: A theoretical and experimental investigation. *Appl. Energy* **281**, 116040 (2021).

23. Merkle, R., Mastrikov, Y. A., Kotomin, E. A., Kuklja, M. M. & Maier, J. First principles calculations of oxygen vacancy formation and migration in $Ba_{1-x}Sr_xCo_{1-y}Fe_yO_{3-\delta}$ perovskites. *J. Electrochem. Soc.* **159**, B219 (2011).
24. Jin, F. et al. CaCo0. 05Mn0. 95O3- δ: a promising perovskite solid solution for solar thermochemical energy storage. *ACS Appl. Mater. Interfaces* **13**, 3856–3866 (2021).
25. Rost, C. M. et al. Entropy-stabilized oxides. *Nat. Commun.* **6**, 1–8 (2015).
26. Gazda, M. et al. Novel class of proton conducting materials—high entropy oxides. *ACS Mater. Lett.* **2**, 1315–1321 (2020).
27. Sharma, Y. et al. Single-crystal high entropy perovskite oxide epitaxial films. *Phys. Rev. Mater.* **2**, 060404 (2018).
28. Jiang, S. et al. A new class of high-entropy perovskite oxides. *Scr. Mater.* **142**, 116–120 (2018).
29. Tezsevin, I., Van De Sanden, M. C. & Er, S. High-throughput computational screening of cubic perovskites for solid oxide fuel cell cathodes. *J. Phys. Chem. Lett.* **12**, 4160–4165 (2021).
30. Gryaznov, D., Finnis, M. W., Evarestov, R. A. & Maier, J. Oxygen vacancy formation energies in Sr-doped complex perovskites: ab initio thermodynamic study. *Solid State Ion.* **254**, 11–16 (2014).
31. Das, T., Nicholas, J. D. & Qi, Y. Polaron size and shape effects on oxygen vacancy interactions in lanthanum strontium ferrite. *J. Mater. Chem. A* **5**, 25031–25043 (2017).
32. Daniels, L. M. et al. Local A-site layering in rare-earth orthochromite perovskites by solution synthesis. *Chem. Eur. J.* **22**, 18362–18367 (2016).
33. Zhang, G. et al. Facile synthesis, magnetic and electric characterization of mixed valence $La_{0.75}K_{0.25}AMnTiO_6$ (A = Sr and Ba) perovskites. *Inorg. Chem.* **56**, 10404–10411 (2017).
34. Wang, L. et al. Enhanced thermochemical water splitting through formation of oxygen vacancy in $La_{0.6}Sr_{0.4}BO_{3-\delta}$ (B = Cr, Mn, Fe, Co, and Ni) Perovskites. *ChemPlusChem* **83**, 924–928 (2018).
35. Sun, W. et al. Enhanced electrical properties of $(Bi_{0.2}Na_{0.2}Ba_{0.2}Ca_{0.2}Sr_{0.2})TiO_3$ high-entropy ceramics prepared by hydrothermal method. *Ceram. Int.* **48**, 19492–19500 (2022).
36. Zhang, P. et al. Reduced lattice thermal conductivity of perovskite-type high-entropy $(Ca_{0.25}Sr_{0.25}Ba_{0.25}RE_{0.25})TiO_3$ ceramics by phonon engineering for thermoelectric applications. *J. Alloys Compd.* **898**, 162858 (2022).
37. Su, L. et al. Direct observation of elemental fluctuation and oxygen octahedral distortion-dependent charge distribution in high entropy oxides. *Nat. Commun.* **13**, 1–10 (2022).
38. Zhang, P. et al. High-entropy $(Ca_{0.2}Sr_{0.2}Ba_{0.2}La_{0.2}2Pb_{0.2})TiO_3$ perovskite ceramics with A-site short-range disorder for thermoelectric applications. *J. Mater. Sci.* **97**, 182–189 (2022).
39. Kotomin, E. et al. First principles calculations of oxygen vacancy formation and migration in mixed conducting $Ba_{0.5}Sr_{0.5}Co_{1-y}FeyO_{3-\delta}$ perovskites. *Solid State Ion.* **188**, 1–5 (2011).
40. Mishra, A., Li, T., Li, F. & Santiso, E. E. Oxygen vacancy creation energy in Mn-containing perovskites: an effective indicator for chemical looping with oxygen uncoupling. *Chem. Mater.* **31**, 689–698 (2018).
41. Rothschild, A., Menesklou, W., Tuller, H. L. & Ivers-Tiffee, E. Electronic structure, defect chemistry, and transport properties of $SrTi_{1-x}Fe_xO_{3-y}$ solid solutions. *Chem. Mater.* **18**, 3651–3659 (2006).
42. Daigle, S. & Brenner, D. Statistical approach to obtaining vacancy formation energies in high-entropy crystals from first principles calculations: Application to a high-entropy diboride. *Phys. Rev. Mater.* **4**, 123602 (2020).
43. Chae, S., Williams, L., Lee, J., Heron, J. T. & Kioupakis, E. Effects of local compositional and structural disorder on vacancy formation in entropy-stabilized oxides from first-principles. *NPJ Comput. Mater.* **8**, 1–7 (2022).
44. Muñoz-García, A. M. et al. Unveiling structure–property relationships in $Sr_2Fe_{1.5}Mo_{0.5}O_{6-\delta}$, an electrode material for symmetric solid oxide fuel cells. *J. Am. Chem. Soc.* **134**, 6826–6833 (2012).
45. Pavone, M., Ritzmann, A. M. & Carter, E. A. Quantum-mechanics-based design principles for solid oxide fuel cell cathode materials. *Energy Environ. Sci.* **4**, 4933–4937 (2011).
46. Das, T., Nicholas, J. D. & Qi, Y. Long-range charge transfer and oxygen vacancy interactions in strontium ferrite. *J. Mater. Chem. A* **5**, 4493–4506 (2017).
47. Lany, S. et al. Monte Carlo simulations of disorder in $ZnSnN_2$ and the effects on the electronic structure. *Phys. Rev. Mater.* **1**, 035401 (2017).
48. Millican, S. L. et al. Predicting oxygen off-stoichiometry and hydrogen incorporation in complex perovskite oxides. *Chem. Mater.* **34**, 510–518 (2022).
49. Wang, Y. et al. Correlation between the structural distortions and thermoelectric characteristics in $La_{1-x}A_xCoO_3$ (A = Ca and Sr). *Inorg. Chem.* **49**, 3216–3223 (2010).
50. Sasaki, S., Prewitt, C. T. & Liebermann, R. C. The crystal structure of $CaGeO_3$ perovskite and the crystal chemistry of the $GdFeO_3$-type perovskites. *Am. Mineral.* **68**, 1189–1198 (1983).
51. Shannon, R. D. Revised effective ionic radii and systematic studies of interatomic distances in halides and chalcogenides. *Acta Crystallogr. A.* **32**, 751–767 (1976).
52. Zhang, X. et al. FeO6 octahedral distortion activates lattice oxygen in perovskite ferrite for methane partial oxidation coupled with CO_2 splitting. *J. Am. Chem. Soc.* **142**, 11540–11549 (2020).
53. Robinson, K., Gibbs, G. & Ribbe, P. Quadratic elongation: a quantitative measure of distortion in coordination polyhedra. *Sci.* **172**, 567–570 (1971).
54. Marezio, M. & Dernier, P. The bond lengths in LaFeO3. *Mater. Res. Bull.* **6**, 23–29 (1971).
55. Marezio, M., Remeika, J. & Dernier, P. The crystal chemistry of the rare earth orthoferrites. *Acta Crystallogr. Sect. B: Struct. Crystallog. Cryst. Chem.* **26**, 2008–2022 (1970).
56. Takeda, T. et al. Metal–semiconductor transition, charge disproportionation, and low-temperature structure of $Ca_{1-x}Sr_xFeO_3$ synthesized under high-oxygen pressure. *Solid State Sci.* **2**, 673–687 (2000).
57. Hayashi, N. et al. BaFeO3: a ferromagnetic iron oxide. *Angew. Chem.* **123**, 12755–12758 (2011).
58. Wright, A. J. et al. From high-entropy ceramics to compositionally-complex ceramics: A case study of fluorite oxides. *J. Eur. Ceram. Soc.* **40**, 2120–2129 (2020).
59. Mayeshiba, T. & Morgan, D. Strain effects on oxygen vacancy formation energy in perovskites. *Solid State Ion.* **311**, 105–117 (2017).
60. Das, T., Nicholas, J. D., Sheldon, B. W. & Qi, Y. Anisotropic chemical strain in cubic ceria due to oxygen-vacancy-induced elastic dipoles. *Phys. Chem. Chem. Phys.* **20**, 15293–15299 (2018).
61. Meredig, B. & Wolverton, C. First-principles thermodynamic framework for the evaluation of thermochemical H_2O-or CO_2-splitting materials. *Phys. Rev. B* **80**, 245119 (2009).
62. Emery, A. A., Saal, J. E., Kirklin, S., Hegde, V. I. & Wolverton, C. High-throughput computational screening of perovskites for thermochemical water splitting applications. *Chem. Mater.* **28**, 5621–5634 (2016).
63. Lany, S. Communication: The electronic entropy of charged defect formation and its impact on thermochemical redox cycles. *J. Chem. Phys.* **148**, 071101 (2018).
64. Ritzmann, A. M., Muñoz-García, A. B., Pavone, M., Keith, J. A. & Carter, E. A. Ab initio DFT+ U analysis of oxygen vacancy formation and migration in $La_{1-x}Sr_xFeO_{3-\delta}$ (x = 0, 0.25, 0.50). *Chem. Mater.* **25**, 3011–3019 (2013).
65. Deml, A. M., Stevanović, V., Muhich, C. L., Musgrave, C. B. & O'Hayre, R. Oxide enthalpy of formation and band gap energy as accurate descriptors of oxygen vacancy formation energetics. *Energy Environ. Sci.* **7**, 1996–2004 (2014).
66. Rowberg, A. J. E., Swift, M. W. & Van de Walle, C. G. Understanding carbon contamination in the proton-conducting zirconates and cerates. *Phys. Chem. Chem. Phys.* **23**, 14205–14211 (2021).
67. Yun, T. G., Heo, Y., Bin Bae, H. & Chung, S. Y. Elucidating intrinsic contribution of d-orbital states to oxygen evolution electrocatalysis in oxides. *Nat. Commun.* **12**, 1–11 (2021).
68. van de Walle, A., Asta, M. D. & Ceder, G. The alloy theoretic automated toolkit: a user guide. *Calphad* **26**, 539–553 (2002).
69. van de Walle, A. Multicomponent multisublattice alloys, nonconfigurational entropy and other additions to the Alloy Theoretic Automated Toolkit. *Calphad* **33**, 266–278 (2009).
70. van de Walle, A. et al. Efficient stochastic generation of special quasirandom structures. *Calphad* **42**, 13–18 (2013).
71. Gautam, G. S., Stechel, E. B. & Carter, E. A. Exploring Ca–Ce–M–O (M= 3d Transition Metal) oxide perovskites for solar thermochemical applications. *Chem. Mater.* **32**, 9964–9982 (2020).
72. Li, W., Jacobs, R. & Morgan, D. Predicting the thermodynamic stability of perovskite oxides using machine learning models. *Comput. Mater. Sci.* **150**, 454–463 (2018).
73. Balachandran, P. V. et al. Predictions of new ABO_3 perovskite compounds by combining machine learning and density functional theory. *Phys. Rev. Mater.* **2**, 043802 (2018).
74. Kresse, G. & Furthmüller, J. Efficient iterative schemes for ab initio total-energy calculations using a plane-wave basis set. *Physical review B* **54**, 11169 (1996).
75. Lee, Y., Kleis, J., Rossmeisl, J. & Morgan, D. Ab initio energetics of $LaBO_3$ (001)(B= Mn, Fe, Co, and Ni) for solid oxide fuel cell cathodes. *Phys. Rev. B* **80**, 224101 (2009).
76. Lee, Y., Kleis, J., Rossmeisl, J., Shao-Horn, Y. & Morgan, D. Prediction of solid oxide fuel cell cathode activity with first-principles descriptors. *Energy Environ. Sci.* **4**, 3966–3970 (2011).
77. Feng, Z. et al. Anomalous interface and surface strontium segregation in $(La_{1-y}Sr_y)_2CoO_{4\pm\delta}/La_{1-x}Sr_xCoO_{3-\delta}$ heterostructured thin films. *J. Phys. Chem. Lett.* **5**, 1027–1034 (2014).
78. Sharan, A. & Lany, S. Computational discovery of stable and metastable ternary oxynitrides. *J. Chem. Phys.* **154**, 234706 (2021).
79. Goyal, A., Zakutayev, A., Stevanović, V. & Lany, S. Computational fermi level engineering and doping-type conversion of $Mg:Ga_2O_3$ via three-step synthesis process. *J. Appl. Phys.* **129**, 245704 (2021).
80. Ong, S. et al. Python Materials Genomics (pymatgen): A robust, open-source python library for materials analysis. *Comput. Mater. Sci.* **68,** 314–319 (2013).

81. Stevanović, V., Lany, S., Zhang, X. & Zunger, A. Correcting density functional theory for accurate predictions of compound enthalpies of formation: Fitted elemental-phase reference energies. *Phys. Rev. B* **85**, 115104 (2012).
82. Sundell, P. G., Björketun, M. & Wahnström, G. Thermodynamics of doping and vacancy formation in $BaZrO_3$ perovskite oxide from density functional calculations. *Phys. Rev. B* **73**, 104112 (2006).
83. Ritzmann, A. M., Pavone, M., Muñoz-García, A. B., Keith, J. A. & Carter, E. A. Ab initio DFT+ U analysis of oxygen transport in $LaCoO_3$: the effect of Co^{3+} magnetic states. *J. Mater. Chem. A* **2**, 8060–8074 (2014).
84. Olsson, E., Aparicio-Anglès, X. & de Leeuw, N. H. Ab initio study of vacancy formation in cubic $LaMnO_3$ and $SmCoO_3$ as cathode materials in solid oxide fuel cells. *J. Chem. Phys.* **145**, 014703 (2016).
85. Lee, Y.-L. & Morgan, D. Ab initio and empirical defect modeling of $LaMnO_{3\pm\delta}$ for solid oxide fuel cell cathodes. *Phys. Chem. Chem. Phys.* **14**, 290–302 (2012).
86. Kuklja, M. M., Mastrikov, Y. A., Jansang, B. & Kotomin, E. A. The intrinsic defects, disordering, and structural stability of $Ba_xSr_{1-x}Co_yFe_{1-y}O_{3-\delta}$ perovskite solid solutions. *J. Phys. Chem. C* **116**, 18605–18611 (2012).
87. Huang, K. *Statistical mechanics*, John Wiley & Sons (2008).

ACKNOWLEDGEMENTS

This work is supported by the U.S. Department of Energy's Office of Energy Efficiency and Renewable Energy (EERE) under Agreement Number DE-EE0008839, managed by the Hydrogen and Fuel Cell Technologies Office in the Fiscal Year 2019 H2@SCALE program. The Alliance for Sustainable Energy, LLC, operates and manages the National Renewable Energy Laboratory for the US. Department of Energy (DOE) under Contract No. DE-AC36-08GO28308. The research was performed using computational resources sponsored by the Department of Energy's Office of Energy Efficiency and Renewable Energy and located at the National Renewable Energy Laboratory and was conducted using computational resources and services at the Center for Computation and Visualization, Brown University.

AUTHOR CONTRIBUTIONS

J.Park performed first principles calculations, analyzed data, and drafted the paper. B.X. contributed to the method development. D.Z. performed the experiments under the supervision of J.L. and X.L.. J.Pan and S.L. assisted analyzing the modeling data. Y.Q. supervised the calculations, model development, and drafted the paper with J.P. and B.X.. All contributors revised the manuscript.

COMPETING INTERESTS

The authors declare no competing interests.

ADDITIONAL INFORMATION

Supplementary information The online version contains supplementary material available at https://doi.org/10.1038/s41524-023-00981-1.

Correspondence and requests for materials should be addressed to Yue Qi.

Reprints and permission information is available at http://www.nature.com/reprints

Publisher's note Springer Nature remains neutral with regard to jurisdictional claims in published maps and institutional affiliations.